# Photocatalytic Degradation of Phenolic Compounds from Wastewater Using Titanium dioxide@reduced Graphene Oxide (TiO₂@rGO) Nanocomposites

*Lu Yu*[*]*, Bo Tang*

School of Chemistry and Chemical Engineering, Henan Institute of Science and Technology, Xinxiang, 453003, China
[*]E-mail: LuYu2021@hotmail.com, iamyl57@163.com

In this work, the synthesis of titanium dioxide@reduced graphene oxide (TiO₂@rGO) nanocomposite as a photocatalyst for the degradation of phenol as a chemical pollutant of industrial wastewater was investigated. XRD, SEM, UV-Vis absorption spectra, and EIS were used to characterize the samples. In TiO₂@rGO, the structural results revealed a significant combination of TiO₂ and rGO. The optical characteristics revealed that Eg values for bare TiO₂ and TiO₂-rGO composites were 3.14 eV and 3.07 eV, respectively, which corresponded to the shrinking band gap value of TiO₂-rGO nanocomposites. Because of the successful inclusion of rGO into the nanocomposite structure and the greater effective surface area, EIS evaluation revealed that TiO₂-rGO had a greater specific capacitance than TiO₂. Under UV irradiation for 35 minutes, photocatalytic tests revealed phenolic degradation efficiencies of 59.2% and 100% for bare TiO₂ and TiO₂-rGO composites, respectively. As a result, rGO considerably increased the degrading efficiency of bare TiO₂. Furthermore, after 30 minutes of visible irradiation, the phenolic degradation efficiencies for bare TiO₂ and TiO₂-rGO composites were 44.1% and 100%, respectively, indicating that visual irradiation promotes the degradation rate for TiO₂-rGO nanocomposites. As a consequence, TiO₂-rGO nanocomposites not only were photoexcited in the UV region but their catalytic efficiency in the visible region was also delayed.

## 1. INTRODUCTION

The well-known pollution sources include three wastes from industrial production, waste gas and residue from fossil energy combustion, waste electronic waste and plastic products, etc., which cause great damage to the atmosphere, water source and soil [1, 2]. But the most closely related to our life is the problem of indoor air pollution. The common indoor air pollution mainly comes from the organic volatile compounds released from decoration materials, coatings and furniture, such as formic

acid, benzene, toluene, etc., which cause serious harm to human health [3]. Traditional treatment methods include activated carbon adsorption, long-term empty ventilation, green plant support, non-equilibrium plasma and ozone purification, but these methods have their shortcomings [4]. Heterogeneous photocatalysis is a rapid development technology in the field of environmental engineering and has been used in many industrial fields, including purification of water sources to remove toxic compounds in water, purification of air for sterilization, conversion of nitrogen compounds into acid salts, self-cleaning surface, etc [5, 6]. Due to its advantages of low cost, simple operation, low energy consumption and wide range of degraded pollutants, photocatalytic technology has been widely concerned and considered as the most promising technology to solve environmental problems [7]. Photocatalysis is a phenomenon that uses light energy to accelerate chemical reactions on catalyst surfaces [8, 9]. Under the action of light, active species are formed on the surface of photocatalyst, which can be digested into harmless end products through an oxidation-reduction reaction with organic or inorganic pollutants [10, 11].

Many industries, such as fungicide-producing plants, paper mills, and herbicides, have phenols and phenolic chemicals in their effluent [12]. Many of them seem to be extremely poisonous, causing harm to both animals and plants [13]. Full mineralization has been obtained under a range of circumstances, demonstrating that photocatalysis is a viable technology for purifying phenolic wastewater [14]. Photocatalytic techniques utilizing $TiO_2$ as catalyst and oxygen as an electron acceptor have been widely documented to degrade phenol [15, 16].

The study and advancement of $TiO_2$-based photocatalyst technologies have been a major problem for scientists for many years [17]. Due to the improved mechanical and chemical durability of $TiO_2$-based photocatalysts, this research have been done via the synthesis of different TiO2 nanostructures and $TiO_2$-based composite and hybrid systems [18]. Nanostructured electrodes with large porosity and effective surface area improve reactivity and sensitivity to visible and UV light and chemical species absorption [19, 20]. Although numerous research has been done to examine the photocatalytic characteristics of semiconductor materials, the $TiO_2@rGO$ nanocomposites have never been examined. As a result, our research focused on the development of a TiO2@rGO nanocomposite for phenolic degradation as organic dyes into industrial wastewater.

## 2. MATERIALS AND METHODS

$TiO_2@rGO$ composites were prepared using a hydrothermal method [21]. To make a 0.5M Ti(IV) solutions, 3.7mL titanium isopropoxide was mixed with 3.3mL triethanolamine inside a 25ml beaker. The $TiO_2@rGO$ composites were made by continuously stirring varying volumes of a GO dispersion into 43mL of water: ethanol (1:14) mixture. After that, 8.6mL of the 0.5M Ti(IV) mixture was taken and stirred at room temperature for 24 hours to form a homogenous solution, which was then put in a 120 mL Teflon vessel within such a steel reactor, and heated at 180°C for 24 hours. The solid was then washed repeatedly with ethanol, centrifuged at 15,000 rpm for 20 minutes, and oven-dried at 70 °C.The same experimental procedure was used to create pure TiO2 samples (without the inclusion of GO) and rGO (without titanium isopropoxide).

The morphology of prepared $TiO_2$@rGO composites was characterized via scanning electron microscopy (SEM). The crystal structure of produced samples was investigated using X-ray diffraction (XRD) at a power of 35 kV and a current of 20 mA at a wavelength of CuKα (λ=1.5418Å). A UV-VIS spectrophotometer was used to examine the optical absorption spectra of the produced samples. Using potentiostat equipment in a typical three-electrode electrochemical cell, EIS studies were conducted in the frequency range of $10^{-3}$ to $10^5$Hz at a pulsed signal amplitude of 5mV. The reference electrode in the electrochemical cell was Ag/AgCl, the counter electrode was Pt wire, and the working electrode was the prepared specimens ($TiO_2$ and $TiO_2$@rGO composites). The electrolyte solution consisted of 0.1M KCl (99%) and a 5mM compound $[Fe(CN)_6]^{3-/4-}$ solution.

The photocatalytic tests were carried out in the presence of bare $TiO_2$ and $TiO_2$@rGO photo-catalysts with an initial concentration of phenol. For the preparation of the standard solution, 0.005, 0.025, 0.05, and 0.1g phenol was put into a 500ml volumetric flask to prepare 10, 50, 100 and 200 mg /L solution, and store at 3-5ºC. The measurements were made in a cylindrical photo-reactor that was exposed to visible and UV light sources. The photo-degradation solution was kept in the dark for 40 min to obtain an adsorption-desorption balance between the phenol solution and the photo-catalysts, and then photocatalytic processes were carried out under light irradiation. Optical absorption spectra obtained with a spectrophotometer at $\lambda$= 663nm were used to assess the change in phenol concentrations. Using the measured absorption intensity of a UV-Vis spectrophotometer at 461nm, the degradation efficiency (%) of phenol was calculated using the following equation [22]:

$$\text{Degradation efficiency} = \frac{I_0 - I_t}{I_0} \times 100 = \frac{C_0 - C_t}{C_0} \times 100 \qquad (1)$$

Where $I_0$ was its phenol solution's initial absorption intensity and $I_t$ is the phenol solution's absorption intensity during irradiation. $C_0$ was its phenol solution concentration before irradiation, and $C_t$ is really the phenol solution concentration after irradiation.

Also, the prepared photocatalyst was applied to wastewater collected from industrial wastewater of Xinxiang, China. The real samples were filtered and centrifuged at 1000rpm, and the supernatant was utilized as real samples to produce the 10mg/l phenol solution.


## 3. RESULTS AND DISCUSSION

Surface morphologies of the rGO and TiO2@rGO nanocomposites are shown in figure 1. As shown in figure 1a, thick massive graphite flakes having inhomogeneity graphitic have appeared on the samples. When combining TiO2 with rGO nanosheets, as indicated in Figure 1b, we find that $TiO_2$ nanoparticles were intimately combined by rGO nanosheets, suggesting the large amount of $TiO_2$ nanoparticles mixed along the surface of rGO.
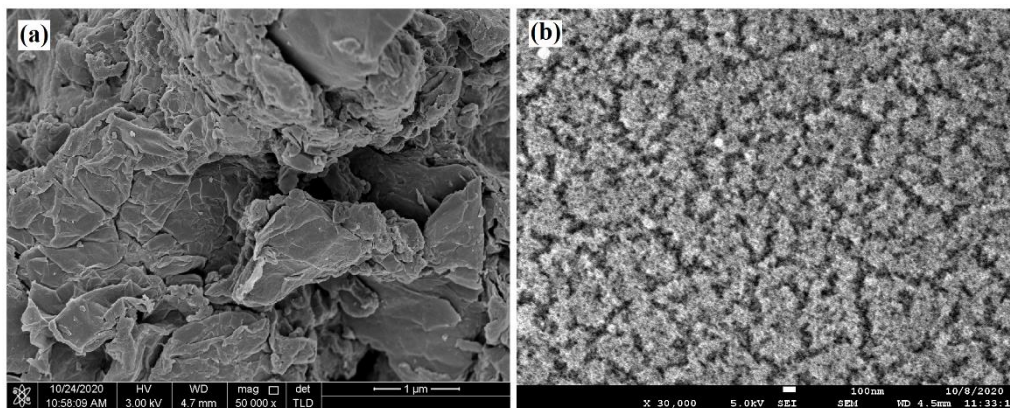
**Figure 1.** FESEM images of the (a) rGO, (b) TiO2@rGO nanocomposites.

XRD patterns ofrGO, $TiO_2$ and $TiO_2$@rGO composites are revealed in Figure 2. The XRD pattern of rGO shows a wide peak centered at 24.47° appears on the rGO sample diffractogram, showing inadequate sheet ordering along its stacking direction [23]. XRD pattern of $TiO_2$ indicates recorded diffraction peaks at $2\theta=25.74°$, 38.05°, 48.02°,54.47°, 62.79°, 69.04° and 75.23° can be related to the (101), (004), (200), (105), (213), (204), (116), and (215) planes, respectively. These planes indicated to the anatase crystal structure of $TiO_2$ (JCPDS card No:21-1272) [24]. Furthermore, at 43.18°, a band formed that matched the turbostratic band of amorphous carbon structures [25]. There were no visible diffraction peaks for rGO in any $TiO_2$@rGO samples (Fig. 2), possibly due to the low percentages of rGO, thus they were masked by the $TiO_2$ diffraction signal, or because the uniform stack of GO was destroyed during specimen preparation by the intercalation of $TiO_2$[26].
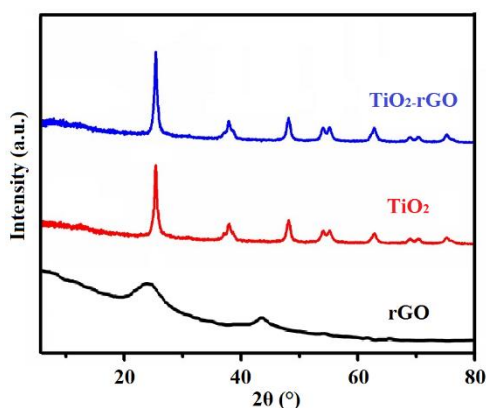


**Figure 2.** XRD patterns ofrGO, $TiO_2$, and $TiO_2$@rGO composites

EIS tests were performed on samples in the frequency range from 0.1Hz to 0.1MHz, with a 5mV applied voltage into 0.1MKCl (99%), incorporating a 5mM complex $[Fe(CN)_6]^{3-/4-}$ solutions.

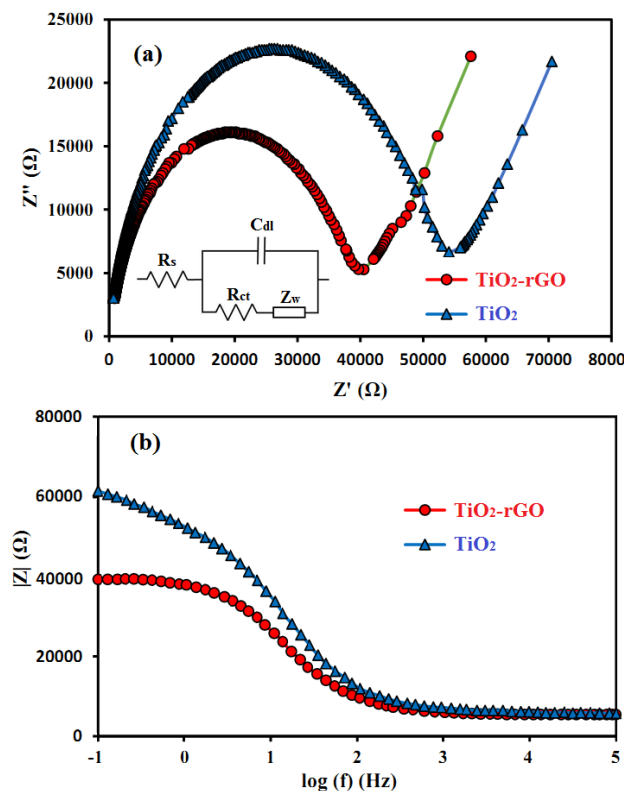**Figure 3. (a)** Nyquist plots and (b) Bode diagrams of $TiO_2$ and $TiO_2$-rGO composites 0.1Hz to 0.1MHz, with a 5mV applied voltage into 0.1MKCl (99%), incorporating a 5mM complex $[Fe(CN)_6]^{3-/4-}$ solutions. Inset of figure 3a shows an equivalent circuit model.

Figure 3 indicates Nyquist plots and (b) Bode diagrams of TiO2 and TiO2-rGO composites. The used Randles circuit, as indicated in the inset of Figure 3a, received the impedance findings. $R_{ct}$ and $C_{dl}$ represent the charge-transfer resistance and double-layer capacitance, respectively [27]. $R_s$ shows the solution resistance.

**Table 1.** Obtained electrochemical parameters

| Samples | $R_s(\Omega \, cm^2)$ | $R_{ct}(k\Omega \, cm^2)$ | $C_{dl}(\mu F \, cm^{-2})$ |
|---|---|---|---|
| $TiO_2$ | 74 | 58.2 | 7.3 |
| $TiO_2$-rGO | 78 | 43.1 | 10.6 |

The nature of all samples is similar, with a semicircle loop at high-frequency and a straight line at low-frequency. The straight line represents diffusion or movement of electrolyte ion to the surface of the electrode, whereas the semicircle represents charge-transfer resistance ($R_{ct}$). As indicated in the table 1, the TiO2-rGO nanocomposites had a lower Rct value than $TiO_2$, which was due to the synergistic action of rGO and $TiO_2$, which resulted in an increase in TiO2 conductivity. Furthermore, a high electron-transfer rate can be related to more rGO-$TiO_2$ interfaces.

Figure 4a shows the recorded absorption spectrum of bare $TiO_2$ and $TiO_2$-rGO composites at room temperature. The absorption edge of $TiO_2$-rGO composites is redshifted toward bare $TiO_2$, which might be attributed to the presence of rGO levels in the $TiO_2$ energy gap decreasing the bandgap energy [28]. This reveals that bare $TiO_2$'s absorption range is confined to the UV region, whereas rGO can increase the photo-activation range of nanocomposites to the visible region [29]. The Tauc equation was used to calculate the optical bandgap (Eg) of the composites, as shown below [30]:

$$(\alpha h\nu)^{\frac{1}{2}} = A(h\nu - E_g) \qquad\qquad (1)$$

Where α represents absorption coefficient, h shows Planck's constant, and ν indicates the light frequency. As shown in Figure 4b, the optical bandgap values are attained 3.14 eV and 3.07 eV for bare $TiO_2$ and $TiO_2$-rGO composites, respectively. The creation of oxygen vacancies can increase the defect's energy level under the valance band and move its edge into the visible region, narrowing the bandgap [31].
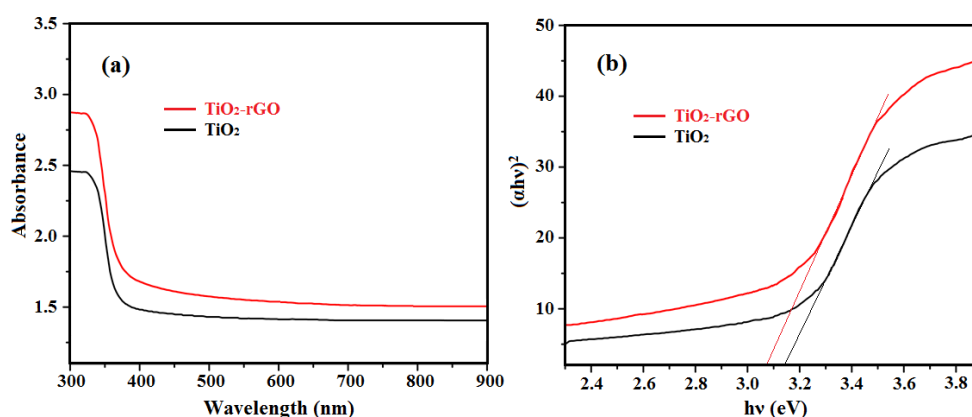


**Figure 4.** (a) The absorption spectrum and (b) the Tauc curves of the bare $TiO_2$ and TiO2-rGO nanocomposites at room temperature.

Under dark and UV light irradiation, Figure 5a illustrates the degradation efficiency of 50mg $l^{-1}$ phenol in the presence of bare $TiO_2$ and $TiO_2$-rGO composites, as well as in the absence of photocatalyst (blank). For 10 mins under dark condition, degradation efficiencies of 0.65 %, 1.97 %, and 2.06 % were achieved for blank, bare $TiO_2$ and $TiO_2$-rGO composite photo-catalysts, respectively. Furthermore, during 35 minutes of UV radiation, the phenolic degradation efficiencies were 1.97%, 59.20%, and 100% for the blank sample, bare $TiO_2$, and $TiO_2$-rGO composites, respectively. As a result, rGO considerably improved the degrading efficiency of $TiO_2$ composites. Figure 5b exhibits the photo-degradation activities of produced photo-catalysts under visible light irradiation, revealing that the phenolic degradation efficiencies for bare $TiO_2$ and $TiO_2$-rGO composites after 30 min of visible light irradiation were 44.10% and 100%, respectively. As a consequence of the comparison between the findings of Figure 5, it is clear that under visible light irradiation, the degradation rate of TiO2-rGO composites is enhanced. This might be due to a decrease in Eg value and a change in the optical characteristics of modified photocatalysts [32]. Furthermore, the development of physical defects as

chemical forms by rGO can increase charge separation by acting as a sponge for trapping photoinduced holes and electrons and slowing their recombination rate [33].
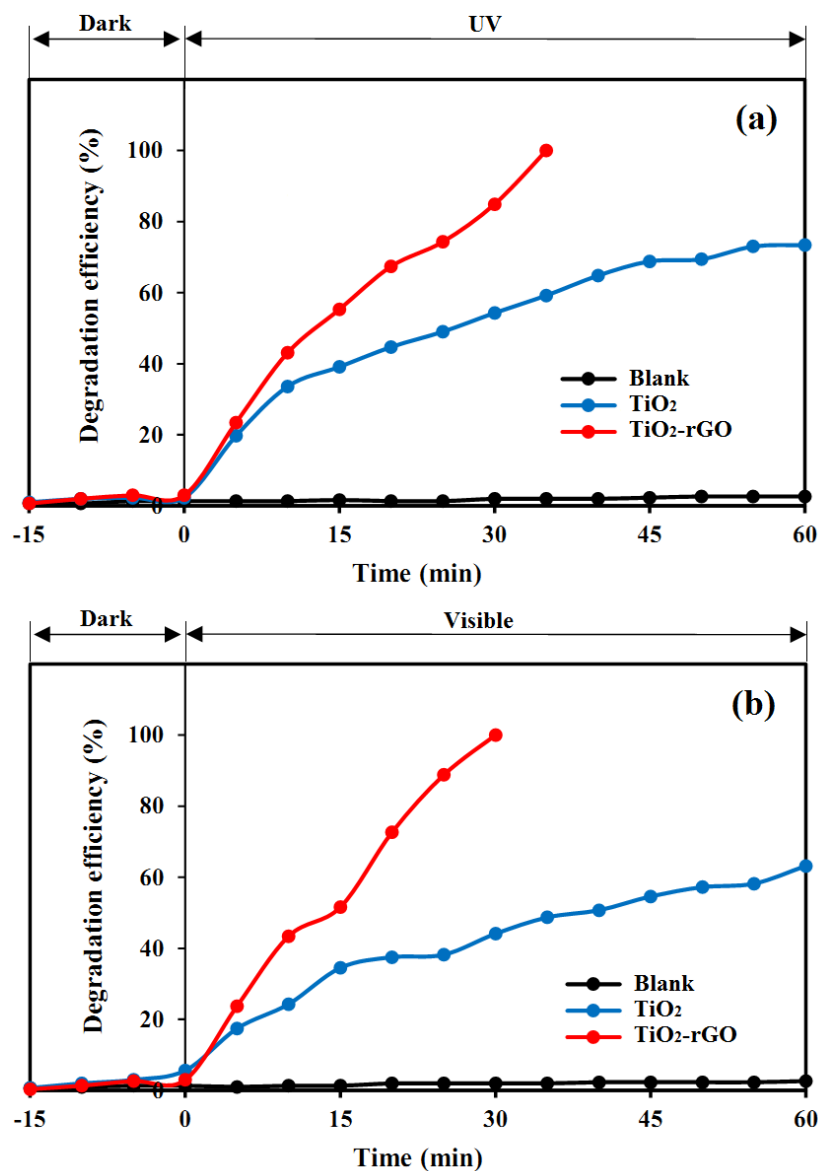


**Figure 5.** Degradation efficiency of 50mg $l^{-1}$ phenol in the presence of bare $TiO_2$ and $TiO_2$-rGO composites, as well as in the absence of photocatalyst (blank) (a) UV irradiation and (b) visible light irradiation.

Figures 6 shows the phenolic degradation efficiency on TiO2-rGO composites for various phenol concentrations under visible and UV irradiations. As can be seen, visible irradiation caused greater photodegradation than UV irradiation. Under UV irradiation, whole degradation for 10, 50, 100, and 200mg $l^{-1}$ of phenol occurs after 30, 35, 65, and 90min, respectively.
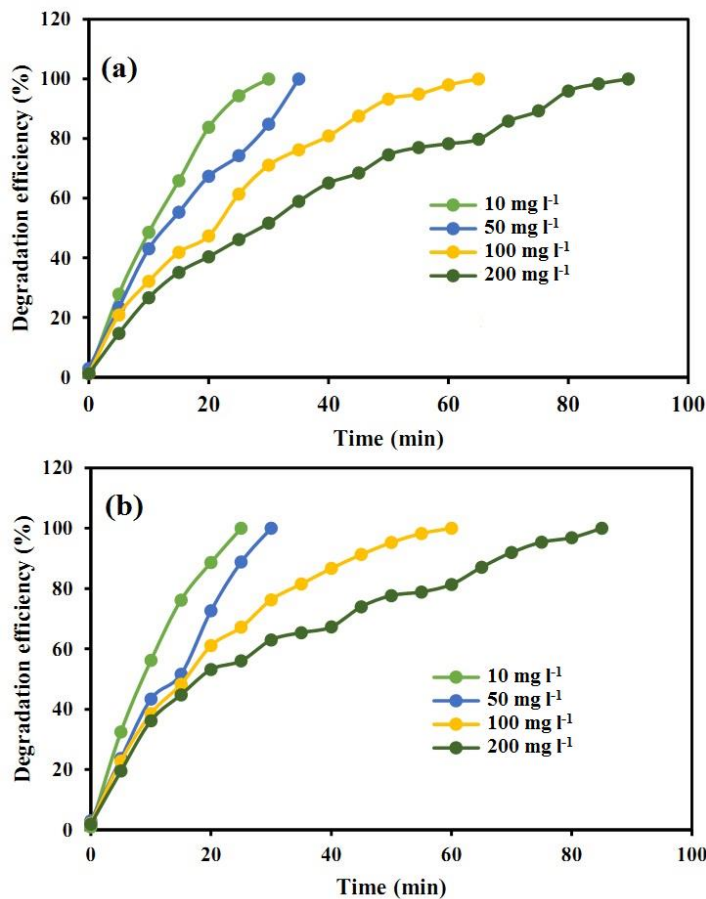
**Figure 6.** Phenolic degradation efficiency on $TiO_2$-rGO composites for various phenol concentrations under (a) UV irradiation and (b) visible light irradiation

**Table 2.** Comparison between the degradation efficiencies of prepared $TiO_2$-rGO composite and other reported photocatalysts for phenolic degradation.

| Photo-catalysts | Phenol concentration(mg $l^{-1}$) | Light sources | Degradation efficiency (%) | Irradiation time (min) | Ref. |
|---|---|---|---|---|---|
| ZnO/rGO nanocomposite | 500 | Sunlight | 92.43 | 120 | [34] |
| Au-Pd-rGO nanocomposite | 200 | Sunlight | 100 | 300 | [35] |
| ZnSnO3/rGO | 50 | Visible | 72.89 | 90 | [36] |
| $TiO_2$/activated carbon | 1000 | Sunlight | 100.0 | 120 | [37] |
| $TiO_2$ nanoparticles | 500 | Visible | 97.0 | 120 | [38] |
| $TiO_2$-rGO composite | 200 | UV | 100.0 | 90 | This work |
|  |  | Visible | 100.0 | 85 |  |

Moreover, under visible irradiation, the whole degradation of 10, 50, 100, and 200mg $l^{-1}$ of phenol were found after 25, 30, 60 and 85 min, respectively. As revealed in table 2, the degrading efficiency of this photocatalyst is compared to the other reported data for phenolic degradation. Under

visible and UV irradiation, the produced $TiO_2$-rGO composites showed enhanced photocatalytic activity for phenolic degradation.

Figure 7 shows the UV–Vis spectra of photocatalytic degradation of 10mg/l phenol prepared from the real sample at various irradiation times by $TiO_2$-rGO composite. It can be seen that the intensity of the absorption peaks at 555nm continuously reduces during the photodegradation reactions which is similar to reported results of phenol degradation over Au-ZnO nanomaterials [39] ana $FeTiO_3$/GO nanocomposite [40]. The peak was disappeared after 90 min degradation of the real sample which consist with results obtained.
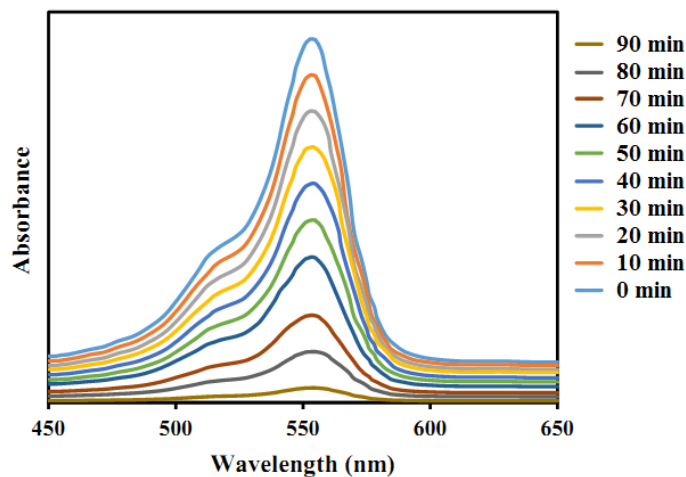


**Figure 7.** UV–Vis spectra of photocatalytic degradation of 10mg/l MO prepared from real sample at different irradiation time by $TiO_2$-rGO composite

## 4. CONCLUSIONS

The $TiO_2$@rGO nanocomposites were synthesized for the degradation of phenol as a chemical pollutant of industrial wastewater was investigated. XRD, SEM, UV-Vis absorption spectra, and EIS were used to characterize the samples. In $TiO_2$@rGO, the structural results revealed a significant combination of $TiO_2$ and rGO. The optical characteristics revealed that Eg values for bare $TiO_2$ and $TiO_2$-rGO composites were 3.14 eV and 3.07 eV, respectively, corresponded to the shrinking band gap value of $TiO_2$-rGO nanocomposites. Because of the successful inclusion of rGO into the nanocomposite structure and the greater effective surface area, EIS evaluation revealed that $TiO_2$-rGO had a greater specific capacitance than $TiO_2$. Under UV irradiation for 35 minutes, photocatalytic tests revealed phenolic degradation efficiencies of 59.2% and 100% for bare TiO2 and TiO2-rGO composites, respectively. As a result, rGO considerably increased the degrading efficiency of bare $TiO_2$. Furthermore, after 30 minutes of visible irradiation, the phenolic degradation efficiencies for bare $TiO_2$ and $TiO_2$-rGO composites were 44.1% and 100%, respectively, indicating that visual irradiation promotes the degradation rate for $TiO_2$-rGO nanocomposites. As a consequence, $TiO_2$-rGO nanocomposites not only were photoexcited in the UV region but their catalytic efficiency in the visible region was also delayed.

**References**

1.  Z. Usmani, M. Sharma, A.K. Awasthi, N. Sivakumar, T. Lukk, L. Pecoraro, V.K. Thakur, D. Roberts, J. Newbold and V.K. Gupta, *Bioresource Technology*, 23 (2020) 124548.
2.  H. Karimi-Maleh, Y. Orooji, A. Ayati, S. Qanbari, B. Tanhaei, F. Karimi, M. Alizadeh, J. Rouhi, L. Fu and M. Sillanpää, *Journal of Molecular Liquids*, 329 (2021) 115062.
3.  N. Carslaw and D. Shaw, *Environmental Science: Processes & Impacts*, 21 (2019) 1313.
4.  M. Domonkos, P. Tichá, J. Trejbal and P. Demo, *Applied Sciences*, 11 (2021) 4809.
5.  N. Pichel, M. Vivar and M. Fuentes, *Chemosphere*, 218 (2019) 1014.
6.  H. Karimi-Maleh, Y. Orooji, F. Karimi, M. Alizadeh, M. Baghayeri, J. Rouhi, S. Tajik, H. Beitollahi, S. Agarwal and V.K. Gupta, *Biosensors and Bioelectronics*, 184 (2021) 113252.
7.  F. Deng, H. Shi, Y. Guo, X. Luo and J. Zhou, *Current Opinion in Green and Sustainable Chemistry*, 13 (2021) 100465.
8.  A. Zada, P. Muhammad, W. Ahmad, Z. Hussain, S. Ali, M. Khan, Q. Khan and M. Maqbool, *Advanced Functional Materials*, 30 (2020) 1906744.
9.  Q. Li, K. Wang, X. Lu, R. Luo, M. Zhang, C. Cui and G. Zhu, *International Journal of Electrochemical Science*, 15 (2020) 9256.
10. A. Akbari, Z. Sabouri, H.A. Hosseini, A. Hashemzadeh, M. Khatami and M. Darroudi, *Inorganic Chemistry Communications*, 115 (2020) 107867.
11. H. Karimi-Maleh, M.L. Yola, N. Atar, Y. Orooji, F. Karimi, P.S. Kumar, J. Rouhi and M. Baghayeri, *Journal of colloid and interface science*, 592 (2021) 174.
12. M. Malakootian and M.R. Heidari, *Water Science and Technology*, 78 (2018) 1260.
13. T.L. DesMarias and M. Costa, *Current opinion in toxicology*, 14 (2019) 1.
14. S.-M. Lam, J.-C. Sin, H. Lin, H. Li, J.W. Lim and H. Zeng, *Applied Surface Science*, 514 (2020) 145945.
15. D. Sánchez-Rodríguez, M.G.M. Medrano, H. Remita and V. Escobar-Barrios, *Journal of environmental chemical engineering*, 6 (2018) 1601.
16. H. Karimi-Maleh, M. Alizadeh, Y. Orooji, F. Karimi, M. Baghayeri, J. Rouhi, S. Tajik, H. Beitollahi, S. Agarwal and V.K. Gupta, *Industrial & Engineering Chemistry Research*, 60 (2021) 816.
17. Z. Xing, J. Zhang, J. Cui, J. Yin, T. Zhao, J. Kuang, Z. Xiu, N. Wan and W. Zhou, *Applied Catalysis B: Environmental*, 225 (2018) 452.
18. S. Riaz and S.-J. Park, *Journal of Industrial and Engineering Chemistry*, 84 (2020) 23.
19. A. Mohammad, M.E. Khan, M.R. Karim and M.H. Cho, *Applied Surface Science*, 495 (2019) 143432.
20. H. Karimi-Maleh, S. Ranjbari, B. Tanhaei, A. Ayati, Y. Orooji, M. Alizadeh, F. Karimi, S. Salmanpour, J. Rouhi and M. Sillanpää, *Environmental Research*, 195 (2021) 110809.
21. B.Y.S. Chang, N.M. Huang, M.N. An'amt, A.R. Marlinda, Y. Norazriena, M.R. Muhamad, I. Harrison, H.N. Lim and C.H. Chia, *International Journal of Nanomedicine*, 7 (2012) 3379.
22. L. Fan, J. Wang, N. Qiu, Y. Liu and X. Zhang, *International Journal of Electrochemical Science*, 14 (2019) 10862.
23. A. Ahmed, M.A. Jalil, M.M. Hossain, M. Moniruzzaman, B. Adak, M.T. Islam, M.S. Parvez and S. Mukhopadhyay, *Journal of Materials Chemistry C*, 8 (2020) 16204.
24. W. Wen, J. Hai, J. Yao, Y.-J. Gu, H. Kobayashi, H. Tian, T. Sun, Q. Chen, P. Yang and C. Geng, *Chemistry of Materials*, 33 (2021) 1489.
25. M. Ruidíaz-Martínez, M.A. Álvarez, M.V. López-Ramón, G. Cruz-Quesada, J. Rivera-Utrilla and M. Sánchez-Polo, *Catalysts*, 10 (2020) 520.
26. K. Alamelu, V. Raja, L. Shiamala and B.J. Ali, *Applied Surface Science*, 430 (2018) 145.
27. H. Dhiflaoui, K. Khlifi, N. Barhoumi and A.B.C. Larbi, *Journal of Materials Research and Technology*, 9 (2020) 5293.

*Int. J. Electrochem. Sci.,* 16 **(2021)** Article ID: 210915

11

28. J.O. Olowoyo, M. Kumar, B. Singh, V.O. Oninla, J.O. Babalola, H. Valdés, A.V. Vorontsov and U. Kumar, *Carbon*, 147 (2019) 385.
29. A.T. Kuvarega and B.B. Mamba, *Critical Reviews in Solid State and Materials Sciences*, 42 (2017) 295.
30. N. Sangiorgi, L. Aversa, R. Tatti, R. Verucchi and A. Sanson, *Optical Materials*, 64 (2017) 18.
31. X. Bi, G. Du, A. Kalam, D. Sun, Y. Yu, Q. Su, B. Xu and A.G. Al-Sehemi, *Chemical Engineering Science*, 234 (2021) 116440.
32. Y. Qin, H. Li, J. Lu, F. Meng, C. Ma, Y. Yan and M. Meng, *Chemical Engineering Journal*, 384 (2020) 123275.
33. M.-f. Li, Y.-g. Liu, G.-m. Zeng, N. Liu and S.-b. Liu, *Chemosphere*, 226 (2019) 360.
34. P.K. Boruah, B. Sharma, I. Karbhal, M.V. Shelke and M.R. Das, *Journal of hazardous materials*, 325 (2017) 90.
35. G. Darabdhara, P.K. Boruah, P. Borthakur, N. Hussain, M.R. Das, T. Ahamad, S.M. Alshehri, V. Malgras, K.C.-W. Wu and Y. Yamauchi, *Nanoscale*, 8 (2016) 8276.
36. G. Gnanamoorthy, V.K. Yadav, D. Latha, V. Karthikeyan and V. Narayanan, *Chemical Physics Letters*, 739 (2020) 137050.
37. M. Gar Alalm, A. Tawfik and S. Ookawara, *Desalination and Water Treatment*, 57 (2016) 835.
38. M.S.F.A. Zamri and N. Sapawe, *Materials Today: Proceedings*, 5 (2018) 21797.
39. J.J. Murcia Mesa, J.A. García Arias, H.A. Rojas and O.E. Cárdenas Espinosa, *Revista Facultad de Ingeniería Universidad de Antioquia*, 16 (2020) 24.
40. M. Moradi, Y. Vasseghian, A. Khataee, M. Harati and H. Arfaeinia, *Separation and Purification Technology*, 261 (2021) 118274.